# Nanostructured Bilayered Vanadium Oxide Electrodes for Rechargeable Sodium-Ion Batteries

**Sanja Tepavcevic,[†] Hui Xiong,[†] Vojislav R. Stamenkovic,[‡,*] Xiaobing Zuo,[§] Mahalingam Balasubramanian,[§] Vitali B. Prakapenka,[⊥] Christopher S. Johnson,[∥,*] and Tijana Rajh[†,*]**

[†]Center for Nanoscale Materials, [‡]Materials Science Division, and [§]X-ray Science Division, Argonne National Laboratory, 9700 South Cass Avenue, Argonne, Illinois 60439, United States, [⊥]Center for Advanced Radiation Sources, University of Chicago, 9700 South Cass Avenue, Argonne, Illinois 60439, United States, and [∥]Chemical Sciences and Engineering, Argonne National Laboratory, 9700 South Cass Avenue, Argonne, Illinois 60439, United States

**ABSTRACT**

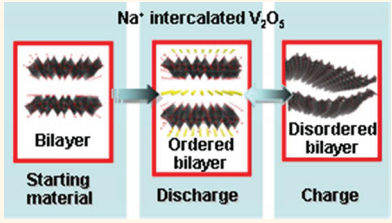


**Tailoring nanoarchitecture of materials offers unprecedented opportunities in utilization of their functional properties. Nanostructures of vanadium oxide, synthesized by electrochemical deposition, are studied as a cathode material for rechargeable Na-ion batteries. *Ex situ* and *in situ* synchrotron characterizations revealed the presence of an electrochemically responsive bilayered structure with adjustable intralayer spacing that accommodates intercalation of $Na^+$ ions. Sodium intake induces organization of overall structure with appearance of both long- and short-range order, while deintercalation is accompanied with the loss of long-range order, whereas short-range order is preserved. Nanostructured electrodes achieve theoretical reversible capacity for $Na_2V_2O_5$ stochiometry of 250 mAh/g. The stability evaluation during charge−discharge cycles at room temperature revealed an efficient 3 V cathode material with superb performance: energy density of ∼760 Wh/kg and power density of 1200 W/kg. These results demonstrate feasibility of development of the ambient temperature Na-ion rechargeable batteries by employment of electrodes with tailored nanoarchitectures.**

**KEYWORDS:** nanostructured electrodes · electrochemical deposition · bilayered $V_2O_5$ · sodium-ion battery

High-performance battery materials are critical for the development of new alternative energy storage systems. While Li-ion batteries are a mature technology for energy storage, disadvantages include cost, Li supply, safety, reliability, and stability. Moreover, the electrolyte stability over time is an additional major concern for long-term operation and advanced applications.[1,2] Thus, the discovery, research, and development of new transporting ions that can provide an alternative choice to Li batteries are essential for further advancement of energy storage materials. Sodium-based batteries are attractive due to the promise of low cost associated with the abundance of sodium and enhanced stability of nonaqueous battery electrolytes due to the lower operating voltages. For those reasons, a broad application of sodium-ion batteries would bring substantial relief and expansion of the existing energy storage market, which is primarily based on Li-ion technology. However, lower voltage leads to insufficient energy density, thus cathode materials for Na batteries must possess high capacities. Since the ionic volume of sodium is about 70% larger than lithium, unique crystalline structures have to be used to accommodate incorporation of large ions.

Vanadium pentoxide ($V_2O_5$) has been intensively studied as the positive electrode material for lithium-ion batteries.[3−6] In previous studies, various fabrication methods were used: sputtering,[7] thermal evaporation,[8,9] thermal decomposition,[6,10] electrophoretic deposition,[11] and many chemical routes, such as hydrothermal synthesis[5,12−14] and sol−gel method.[15] It has been reported that chemical composition, crystal structure, and crystallinity of $V_2O_5$ may have pivotal roles in lithium-ion intercalation capacity and cycling stability.[4] The growing body of experimental results for $V_2O_5$ in lithium-ion batteries indicated that nanodimensional materials could have improved electrochemical properties compared to their bulk counterparts.[3,10,16,17] Some of the enhanced properties are reactivity toward lithium, suppression of phase transformations to improve electrochemical reversibility, and the use of defects and high surface area to produce high capacity for

* Address correspondence to vrstamenkovic@anl.gov, cjohnson@anl.gov, rajh@anl.gov.

Received for review October 7, 2011 and accepted December 12, 2011.

**Published online December 12, 2011**
**10.1021/nn203869a**

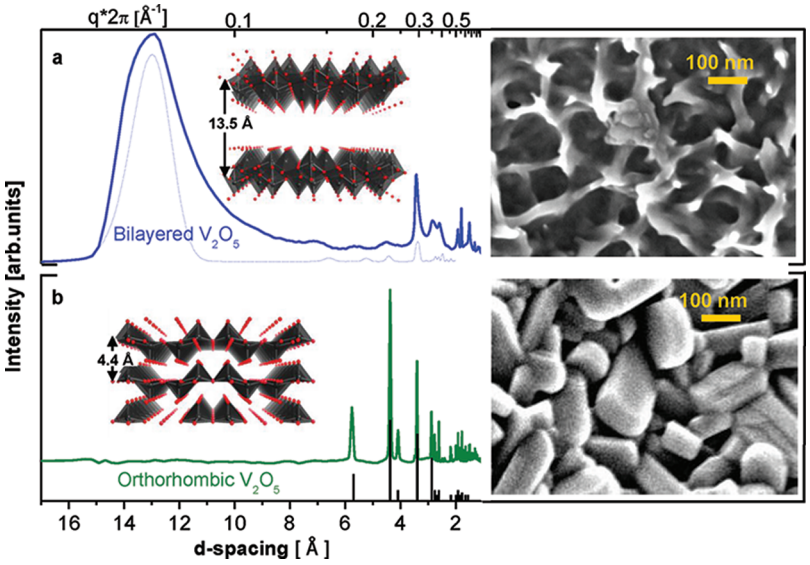


**Figure 1. Synchrotron X-ray diffraction, scanning electron microscopy, and molecular simulations of electrodeposited vanadium oxide: (a) bilayered $V_2O_5$ annealed in vacuum at 120 °C (blue) in conjunction with diffraction simulation (dotted blue) based on the model of monoclinic base-faced bipyramidal layered structure with lattice parameters $a$ = 11.65 Å, $b$ = 3.68 Å, and $c$ = 13.5 Å with $\beta$ = 88.63° depicted in the inset; and (b) orthorhombic $V_2O_5$ annealed in oxygen at 500 °C (green). In each case, $V_2O_5$ was deposited at an anodic current density of 5 mA cm$^{-2}$. Bottom line: spectrum (black) represents standard XRD of orthorhombic $V_2O_5$, JCPDS card #001-0359.**

intercalation of lithium ions.[18] In addition, short diffusion length in nanodimensional materials might be also beneficial for electrode rate capability.[4] However, even with optimized nanostructures and crystallinity, the practical application of vanadium oxides in lithium-ion batteries was still limited due to the poor cycling stability and phase transitions to inactive materials.[6]

The research dedicated to room temperature sodium-ion batteries is still in infancy. Recently, Cao and co-workers[19] reported that single-crystalline nanowires of $Na_4Mn_9O_{18}$ possess promising properties as a cathode for Na-ion battery. A report of Liu *et al.*[20] considered utilization of vanadium oxide by insertion/deinsertion of sodium ion into the $NaV_6O_{15}$ nanorods, while Su *et al.*[21] studied the diffusion coefficient of Na in $V_2O_5$ thin films. Even though the morphology of the material could be retained, the initial discharge capacity of 142 mAh/g substantially decreased by cycling at higher current densities, which led to poor overall performance. Growing body of knowledge related to materials that are suitable for application in Na-ion batteries suggests that both (i) tailoring nanoarchitecture of materials offers unprecedented opportunities in utilization of their functional properties, and (ii) in order to explore full potential in utilization of nanostructured materials, a fundamental insight is necessary. Our approach to achieving sodium intercalation is to use nanoscale materials that have adjustable *d* spacing and two-dimensional layered structure that can accommodate large volume changes. Furthermore, to facilitate reversible insertion of sodium ions, the host lattice that has short-range order would be preferred to crystalline structures due to the conservation of low-entropic energy associated with ordering of intercalated atoms. For that reason, we thoroughly examined the crystalline short-range ordered bilayered $V_2O_5$ and orthorhombic $V_2O_5$ nanostructures. In this report, electrochemically grown nanostructured bilayered vanadium pentoxide is presented as a highly efficient 3 V cathode material for rechargeable sodium-ion batteries. With capacity of 250 mAh/g, excellent rate capability, and cycle life, as well as high energy and power densities of 760 Wh/kg and 1200 W/kg, respectively, this material can be used in advanced energy storage applications at ambient temperature.

## RESULTS AND DISCUSSION

Vanadium pentoxide was synthesized by electrochemical deposition from aqueous vanadyl sulfate electrolyte on Ni foil substrate, and then annealed in vacuum at 120 °C to remove intercalated water. Electrochemically synthesized electrodes offer long-range electronic conductivity, which improves responsiveness to applied potential and, therefore, their intercalation properties. Utilization of electrochemical deposition also brings a high level of control to the structure, morphology, and uniformity of electrodes by adjusting the crucial parameters such as applied current, potential, electric pulses, as well as the temperature and concentration of the electrolyte. In addition, the vanadium oxide electrode is deposited directly on a current collector without the use of an conductive additives (such as carbon black or nickel powder) and/or a polymer binder (such as polyvinylidene difluoride). On the basis of the scanning electron micrograph (Figure 1, top right), such a $V_2O_5$ electrode

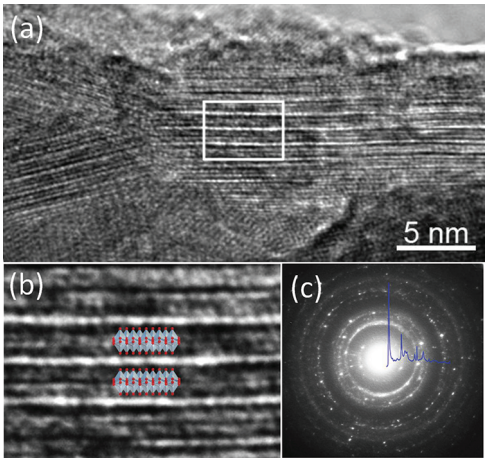


**Figure 2. (a) HRTEM image of electrochemically grown $V_2O_5$ vacuum annealed at 120 °C and (b) the image section shown in the rectangle area in conjunction with the lattice model of monoclinic bilayered base-facing square-pyramidal $V_2O_5$ with lattice parameters $a$ = 11.65 Å, $b$ = 3.68 Å, and $c$ = 11.5 Å with $\beta$ = 88.63°. (c) Electron nanodiffraction of the selected area shown in (a) in conjunction with corresponding XRD diffraction represented in the reciprocal space (blue line).**

is found to be composed of nanoribbons with highly porous structure. The electrochemically grown interconnected ribbons allow excellent electronic conductivity, while the high porosity enables efficient penetration of the electrolyte and ensures high utilization of electrode material. The electrode with such morphology represents an efficient matrix for ion transport in which a high surface area of the electrode diminishes limitations caused by diffusion. The result from synchrotron X-ray diffraction (XRD) (Figure 1a) suggests that the $V_2O_5$ structure is composed of 2D bilayered stacks indicated by narrow features in the intermediate and low $d$ spacing range of the difractogram. These bilayered stacks are separated by large interlayer spacing, which is shown as an intense broad peak at high $d$ spacing (~13.5 Å). The pattern contains a small number of Bragg-like features, indicating the presence of intermediate range ordering and a pronounced diffused component. The bilayered $V_2O_5$ is reminiscent of the $V_2O_5$ xerogels in which monoclinic bilayers of $V_2O_5$ stack up with the spacing that expands (or contracts) as the xerogel incorporates (releases) water molecules.[22,23] This structure is a stacking of $V_2O_5$ bilayers made of base-faced square-pyramidal $VO_5$ units arranged in parallel at equidistant positions (model in Figure 1a). The distance of the closest approach between the bilayer stacks is approximately ~13.5 Å. This is the most noticeable period of repetition in the structure as manifested by the strength and position of the low-angle peak in the XRD pattern. The width of this feature suggests that the stacking sequence is imperfect, confirming disordering in this system. The high-angle domain region is dominated by one peak at 3.44 Å, which is also the highest intensity peak in the simulated diffraction of a monoclinic bilayered model structure and corresponds to the combined diffraction of 201 and 111 planes composed of 2.85 Å apart single layers (Figure 1a, dotted blue line).

The composition of the bilayered structure was additionally investigated by using HRTEM and was found to be in perfect agreement with our XRD studies. Figure 2 shows the HRTEM image of electrochemically grown $V_2O_5$ annealed at 120 °C in conjunction with the lattice model of monoclinic bilayered structure composed of a base-faced square-pyramidal structure of $V_2O_5$, electron nanodiffraction with superimposed XRD (blue curve, Figure 1a) pattern in reciprocal space. We find that the sample is composed of interwoven single-crystalline rods composed of bilayered $V_2O_5$ structure. The interlayer gap shows as the brightest and thickest feature, while two bright layers between the bilayer feature correspond to the spacing between terminating oxygen atoms and the central plane composed of the vanadium and oxygen atoms that form a base of base-faced square-pyramidal $VO_5$. In agreement with XRD, the periodicity of the gap that determines the $c$-axes of the bilayered crystalline unit ranges from 11.5 (Figure 2) to 13.0 Å (Figure S1, Supporting Information) depending on the rod domain and orientation. The size of the gap defined as the spacing between terminating oxygen atoms was found to be ~5.9 Å, and the intralayer distance between the pyramid base and terminating oxygen atoms was found to be ~3.4 Å. The electron nanodiffraction shows the presence of preferred orientation in the crystallinity, as shown by the presence of anisotropic diffraction lines. Electron diffraction pattern (Figure 2c) is in the close agreement with reciprocal space XRD data for bilayered $V_2O_5$ (blue curve) shown in Figure 1a.

When electrochemically grown $V_2O_5$ is annealed in oxygen atmosphere at 500 °C, the SEM image revealed that nanoribbons were converted to fine rod-like shape that exhibit orthorhombic crystalline structure (Figure 1b). On the basis of diffraction patterns and simulated model structure, the orthorhombic phase consisted of single layers of $VO_5$ square pyramids, while the interlayer spacing in the $z$-direction is almost completely diminished compared to bilayered $V_2O_5$, reaching only 4.4 Å.

Considering these findings, the crucial question is which one of these structures supports better the reversible intercalation of sodium transporting ions. While bilayered structure is atomically ordered only in a short-range, the spacing between bilayers is more random. However, there is a lot of void space between randomly spaced bilayers after removal of intercalated water, which, if flexible enough, can readjust the spacing to enable intercalation of larger $Na^+$ ions (model, Figure 1a). On the other hand, orthorhombic rod-like crystals have long-range order that may enable unhindered diffusion of intercalated ions throughout

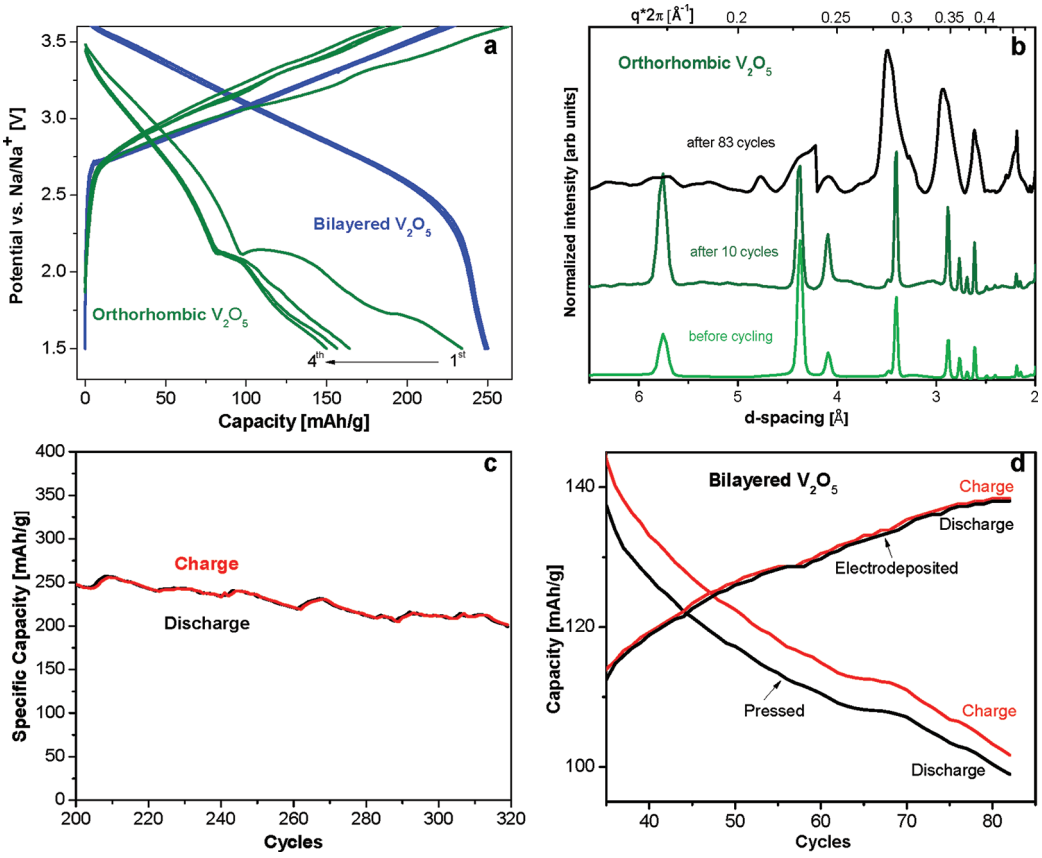


**Figure 3. (a) First four charge−discharge cycles of bilayered $V_2O_5$ and orthorhombic $V_2O_5$ electrodes. Both cells were cycled at 20 mA/g, within the potential window of 3.8−1.5 V (*vs* $Na/Na^+$) from 1 M $NaClO_4$ in PC. (b) *Ex situ* synchrotron XRD patterns of orthorhombic $V_2O_5$ before and after cycling with Na ions: after 10 and after 83 cycles. All films were deposited at an anodic current density of 5 mA $cm^{-2}$. (c) Cycle life of bilayered $V_2O_5$ electrodes. (d) Cycling performance comparison of the same electrochemically grown bilayered $V_2O_5$ film: deposited on Ni substrate and pressed on stainless steel mesh current collector. Both cells were cycled at 630 mA/g current densities, within the potential window of 3.8−1.5 V (*vs* $Na/Na^+$) from 1 M $NaClO_4$ in PC.**

the entire structure that could lead to highly reversible capacity. In order to evaluate functionality of these materials, each type of structure was prepared and was submitted to cycling against sodium metal anode (Figure 3a). Both electrodes exhibited observable capacities; however, the bilayered $V_2O_5$ electrode demonstrates higher electrochemical activity and stable reversible capacity on repeated cycling than its orthorhombic counterpart. In the 3.8 to 1.5 V range, we observe significantly larger specific capacity of 250 mAh/g at 20 mA/g (*C*/8; *C*/*n*, discharge rate in *n* hours) for bilayered $V_2O_5$ electrode compared to only 150 mAh/g for orthorhombic $V_2O_5$. The high capacity of bilayered $V_2O_5$ is comparable to the theoretical limit of 236 mAh/g for $Na_2V_2O_5$, suggesting that this structure can accommodate close to one $Na^+$ ion for each V atom. The cycling curve is composed of two distinct parts: the first with a smooth slope indicative of solid solution intercalation mechanism that reaches ~235 mAh/g (theoretical capacity), and the second one at potentials >2.25 V when the slope changes to a steep curve indicative of capacitative mechanism. This small contribution of 15 mAh/g might be due to the capacitance of the surface layer or due to the presence of small amount of NiO formed at the interface between $V_2O_5$ and Ni substrate during the electrochemical deposition. Moreover, the shape of galvanostatic curves in Figure 3a reveals an entirely different mechanism of intercalation of $Na^+$ transporting ions in two different $V_2O_5$ structures. Incorporation of $Na^+$ ions into the orthorhombic electrode is accompanied with two phase transitions, manifested by the existence of two plateaus both in the discharge and charge cycles, suggesting that the orthorhombic crystalline structure changes twice to accommodate increasing $Na^+$ concentration. On the other hand, the incorporation of $Na^+$ ions into bilayered structure shows smooth, solid state solution intercalation with no phase transitions. Importantly, the capacity of bilayered $V_2O_5$ does not change with cycling including the first cycle. This behavior indicates that there is no side reactions of injected electrons with either electrolyte or surface of nanocrystalline bilayered $V_2O_5$. In contrast, the capacity of orthorhombic electrode rapidly decreases with cycling, as previously reported.[20] The phase transformation in the orthorhombic crystalline electrode is less pronounced as the cycling proceeds

concomitantly with the decrease of the electrode capacity. This behavior suggests that the change in crystalline structure is associated with the fading of the orthorhombic electrode performance. Indeed, examination of XRD patterns with cycling reveals that orthorhombic $V_2O_5$ experienced deterioration in its crystallinity after the first 10 cycles, which is followed by loss of crystallinity after prolonged cycling (Figure 3b). After 82 cycles, the broadening and disappearance of the peaks, especially in longer *d* spacing range (>4 Å), shows significant reduction of the crystalline domains from a few hundred to only a few nanometers. Reduction of the domains of crystallinity is accompanied with loss of the electronic conductivity that directly causes loss of electrode capacity.

On the other hand, bilayered $V_2O_5$ electrodes were stable to repeated cycling and during prolonged galvanostatic cycling (up to 350 cycles, the extent of our study). When the sample was cycled at different rates, the first 30 cycles at 20 mA/g, then 170 cycles at high current density ranging from 60 to 630 mA/g, followed by 120 cycles at slow rate at 20 mA/g, the average capacity of bilayered $V_2O_5$ electrodes remains at 85% of its initial value (Figure 3c). Furthermore, nanostructured bilayered $V_2O_5$ electrodes exhibited excellent discharge capacity and cycle stability even at high-rate charge−discharge processes; for example, the discharge capacity at faster cycling rate of 60 mA/g decreases slightly to 200 mAh/g, while at a rate of 630 mA/g (6 min discharge), it decreases to 150 mA/g. Figure 3d compares charge−discharge performance at fast cycling (630 mA/g) of bilayered $V_2O_5$ prepared electrochemically *versus* mechanically pressed on stainless steel mesh. Interestingly, the bilayered electrode that is electrochemically grown on the Ni substrate shows improvement of the electrode capacity with the cycling (Figure 3d), most likely due to improved supply of $Na^+$ ions through the nanoporous electrode. For comparison, when bilayered $V_2O_5$ was peeled from the Ni substrate, mixed with conductive carbon additive and polymer binder, and pressed on a stainless steel mesh current collector, initial capacity immediately reaches maximal capacity of 140 mAh/g, but substantially decreases by prolonged cycling. This underlines the importance of superior electronic contact and excellent ionic conductivity that is obtained by electrochemical deposition, which are key factors in the stable and reversible operation of batteries. The monotonic slope of the bilayered $V_2O_5$ voltage profiles confirms the absence of phase transitions during the charge−discharge processes (Figure 3a). The results indicate that the bilayered $V_2O_5$ structure is capable of sustaining single-phase intercalation of large $Na^+$ ions in a wide concentration range and does not change morphology during repeated cycling (Figure S2, Supporting Information). These findings suggest the advantage of short-range ordered structures that are far away from the thermodynamic equilibrium for applications in batteries operating on sodium-ion exchange.

Oxidation state of material is essential for redox processes that are taking place in rechargeable batteries, and for that reason, we utilize X-ray absorption near-edge spectra (XANES) in the V *K*-edge range for the bilayered $V_2O_5$, orthorhombic $V_2O_5$ ($V^{5+}$ standard), and $VO_2$ ($V^{4+}$ standard). The obtained values are consistent with the previous results of $V_2O_5$ compounds[24,25] and show identical pre-edge shape and peak positions, implying that the V redox state in the bilayered $V_2O_5$ sample is close to $V^{5+}$, in a common $VO_5$ environment (Figure 4a). However, the area of the pre-edge peak for the bilayered is smaller than that of orthorhombic $V_2O_5$ electrode. These variations in the area of the pre-edge peak indicate that the local structure of V in bilayered $V_2O_5$ has a higher degree of local symmetry than that of V in orthorhombic $V_2O_5$.[26] However, comparison of the V *K*-edge $k^3$-weighted EXAFS spectra shows important differences (Figure 4b). The first two peaks in the V *K*-edge $k^3$-weighted EXAFS are dominated by single scattering contributions from the first and second coordination spheres of V−O and V−V correlations. The scattering contributions of V−O bond in orthorhombic $V_2O_5$ are split into two components, one shorter bond distance (V−O), comparable to distances within square-pyramidal environment, and a longer V−O* distance with major contribution from oxygen atoms from the neighboring planes in the orthorhombic structure.[27] This longer bond distance is absent in Fourier transform spectra of the bilayered structure due to the shorter bond between V and O atoms in base-faced square-pyramidal arrangement. The position and shape of the V 2p and O 1s XPS peaks before and after cycling of bilayered $V_2O_5$ electrodes confirm the reversibility of $Na^+$ intercalation (Figure 4c). The peak at 516.9 eV is assigned to the $V^{5+}$ $2p_{3/2}$, with a shoulder at 515.7 eV to the $V^{4+}$ $2p_{3/2}$ orbital, which is additionally confirmed by the spin−orbit splitting of about 7.5 eV between V $2p_{3/2}$ and V $2p_{1/2}$ (Figure S3, Supporting Information).[7] Composition of the electrochemically synthesized bilayered $V_2O_5$ electrode before the intercalation of $Na^+$ shows slightly reduced content of V, indicated by 25% of total vanadium in $V^{4+}$. However, after 82 cycles, V $2p_{3/2}$ peak shape for the sample in a charged (oxidized) state constitutes 95% of $V^{5+}$ and 5% of $V^{4+}$ state, confirming efficient reversible intercalation and deintercalation of $Na^+$ ions in the bilayered $V_2O_5$ structure.

In the O 1s region, the main peak attributed to lattice oxygen (O−V) is located at 531 eV; however, we observe an additional shoulder at the higher binding energy side in electrochemically synthesized $V_2O_5$, which was previously assigned to chemisorbed water or adsorbed carbon dioxide molecules.[28] This side peak shifts upon cycling, suggesting surface adsorption of

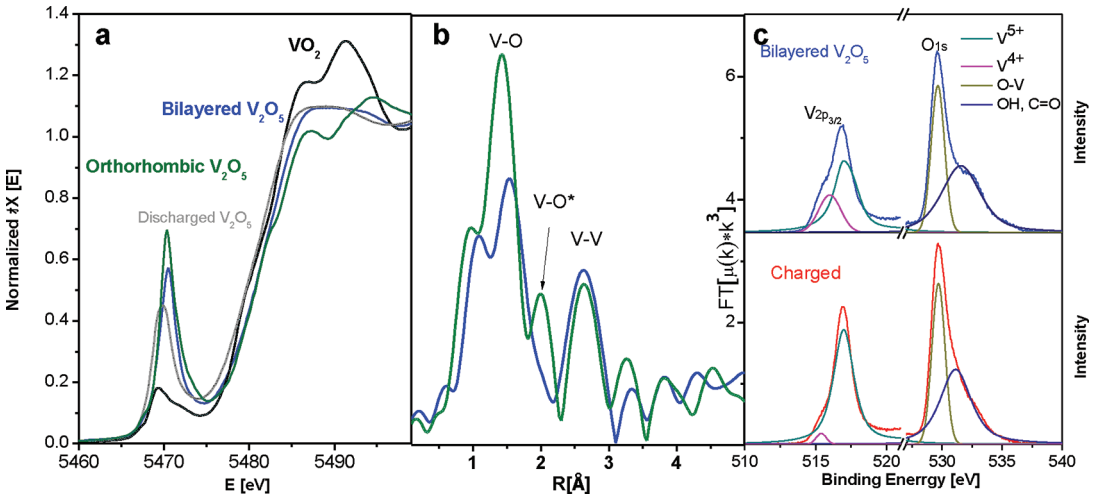


**Figure 4. (a) Normalized V *K*-edge XANES for $VO_2$ ($V^{4+}$ standard), bilayered $V_2O_5$, discharged bilayered $V_2O_5$, and orthorhombic $V_2O_5$ ($V^{5+}$ standard) electrodes. (b) Phase-uncorrected Fourier transforms of V *K*-edge EXAFS ($k^3$-weighted) for bilayered $V_2O_5$ and orthorhombic $V_2O_5$ electrodes. (c) XPS spectra of bilayered $V_2O_5$, before (top) and after 10 cycles of charging with $Na^+$ ions (bottom) in the V $2p_{3/2}$ and O 1s core level regions.**

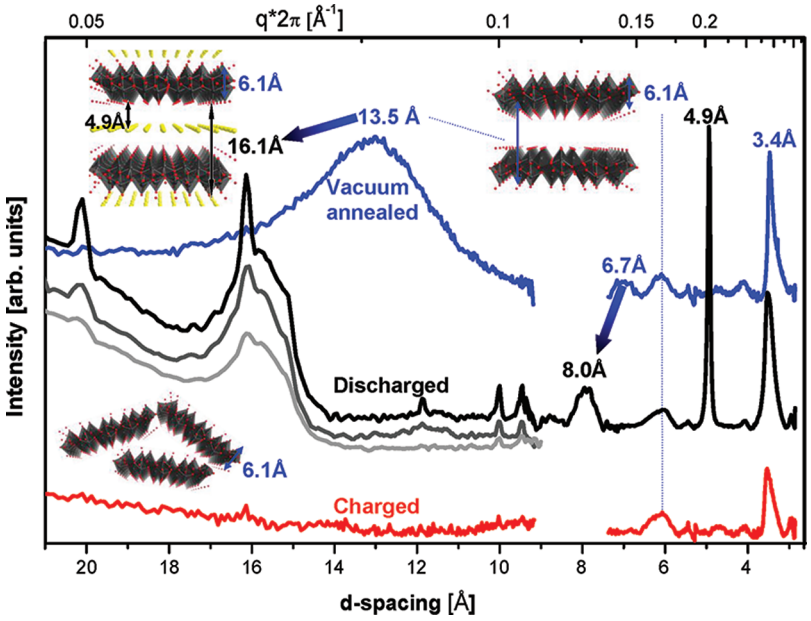


**Figure 5. SAXS and WAXS spectra for bilayered $V_2O_5$: electrochemically deposited vacuum annealed sample (blue); after discharging with the current of 630 $\mu$A (black), 120 $\mu$A(gray), 20 $\mu$A (light gray); and after cycling at 120 $\mu$A in charge state (red). Model structures and critical interlayer spacing depicting transformations occurring upon $Na^+$ intercalation and deintercalation are also shown.**

electrolyte molecules that replace initially adsorbed carbon dioxide during electrode cycling.

In order to understand mechanism of sodium insertion/deinsertion as well as the limits of discharge capacity and cyclability of bilayered $V_2O_5$ electrodes, it is important to understand the response of the bilayered $V_2O_5$ structure to the intercalation of sodium. For this purpose, we have used X-ray scattering that is a technique of choice for determining the changes in both short and long-range order in crystalline and noncrystalline materials. Small and Wide angle X-ray scattering (SAXS and WAXS) measurements *in situ* (non-*operando*) confirm the initial structure of vacuum annealed bilayered $V_2O_5$ that was obtained from XRD measurements, i.e., layered structure with bilayers spaced at average distance of 13.5 Å apart, and the structural order within bilayers showing characteristic 3.44 Å spacing (Figure 5, blue curve). SAXS measurements confirm the change of periodicity and the stacking order upon intercalation and deintercalation of $Na^+$ ions.

Upon initial discharging, we observe that the interlayer *d* spacing of the (001) plane (13.5 Å) and corresponding (002) plane (6.7 Å) dramatically changes

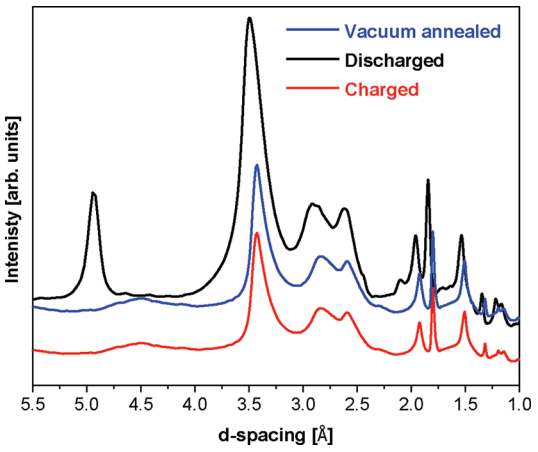


**Figure 6. Synchrotron XRD spectra of bilayered $V_2O_5$ annealed in vacuum at 120 °C (blue), in discharge after $Na^+$-ion intercalation (black) and in charged state after $Na^+$-ion deintercalation (red). In each case, $V_2O_5$ was deposited at an anodic current density of 5 mA $cm^{-2}$.**

upon intercalation of sodium to 16.1 and 8.0 Å, respectively. Concomitantly, the width of the layer spacing peak narrows, and several peaks in the wide-angle region sharpen, suggesting 3D-like ordering of the structure upon sodium intercalation. Moreover, superimposed to the broader scattering pattern corresponding to newly developed sodium-ion assembled layered structure, one can observe a set of very narrow peaks, which originate from defined distances of the intercalated sodium atom with atoms constituting the $V_2O_5$ bilayer. The intensity of these sharp features depends on the applied discharge currents (Figure 5, black and gray curves). One can observe an exceptionally strong narrow peak at 4.9 Å that corresponds to the distance between intercalated $Na^+$ ions and neighboring oxygen atoms that terminate the bilayered structure, which was also observed in the XRD of the discharged sample (Figure 6). Upon electrode oxidation (charging) and consequent $Na^+$ deintercalation, this peak completely vanishes, confirming complete removal of Na ions in agreement with XPS restoration of the $V^{5+}$ state. Also, all of the peaks associated with the layered structure disappear and only those associated with short-range order within the bilayered structure are preserved.

This suggests that after deintercalation of $Na^+$ ions from the structure the stacking order is removed (Figure 5, red curve). These measurements strongly advocate that bilayered stacking and large spacing of bilayered structure is crucial for efficiency and stability of reversible $Na^+$ ion intercalation in $V_2O_5$ electrodes. These flexible noncrystalline layers reassemble into organized structure each time $Na^+$ ions intercalate into the electrode. Electrostatic interaction between sodium ions and bilayer terminating oxygen atoms fixates the stacking of bilayers. However, upon oxidation (charging), the electron density of terminating oxygen atoms decreases, weakening their interaction with $Na^+$ ions that causes deintercalation of $Na^+$, which leaves random ordering between the layers.

XRD studies confirm SAXS and WAXS findings and in addition give further information on the bond lengths and ordering within the bilayer structure during intercalation and deintercalation of Na ions (discharge and charge state of the sample). Figure 6 shows the XRD of $V_2O_5$ in the *d* spacing range from 6 to 1 Å, the range that focuses on intralayer structure. Close inspection of XRD spectra shows that upon intercalation the size of the crystalline unit cell changes slightly (blue to black curve, Figure 6), and we observe that bond lengths within the bilayer structure increase for 1.5−2.5%, depending on the crystalline orientation, in order to accommodate for the presence of Na ions. However, upon deintercalation (black to red curve, Figure 6), the process reverses, and the crystalline unit cell contracts to the size it had before intercalations. It should be noted that the crystallinity of the materials does not decay upon cycling and the crystallinity of the sample is unperturbed even after 80 cycles (red curve, Figure 6). The extent of ordering and corresponding intensity of scattering features is dependent on the current density used for intercalation of $Na^+$ ions (gray curves, Figure 5). Interestingly, the highest current leads to more pronounced peaks, suggesting that higher concentration (flux) of intercalated atoms produces better ordering of the lattice. Moreover, the specific capacity of fast cycled electrode improves with the cycling. The full capacity of this electrode is established only after a number of cycles at high scanning rate, emphasizing the importance of availability of $Na^+$ ions on the electrode surface for obtaining theoretical capacities. Therefore, the superior discharge capacity retention of bilayered $V_2O_5$ electrodes compared to the other nanostructured vanadium pentoxide electrode reported in the literature may be attributed to the combined effects of their structural and surface properties. Highly accessible nanoscale architecture that combines conductivity with high surface area plays a crucial role for ion and electron transport at the electrode/electrolyte interface. It has been shown recently that the increased number of electrode/electrolyte interfacial interactions in nanostructured materials is critical to the formation of percolation pathways for fast diffusion of ions.[29] Extensive adsorption of large sodium ions at the nanostructured electrochemical interface is important to initiate the intercalation process. At the same time, the layered nature of the active material with low-energy sites drives the $Na^+$ diffusion into the material bulk structure. The combination of these processes is necessary for maximizing the flow of $Na^+$ ions into the material. The net effect is enhanced pseudocapacitance that maximizes the electrostatic attraction of $Na^+$ cations into the $V_2O_5$ matrix. In addition, charge transfer ability of the bilayered $V_2O_5$

electrode is improved with the presence of more conductive surface defect species such as lower valence vanadium atoms (Figure 4c) and associated oxygen vacancies. Enhanced charge transfer conductivity improves electron transport during sodium-ion intercalation/deintercalation at the electrode/electrolyte interface. Undoubtedly, this is sufficient to stimulate efficient diffusion of the large concentration of transporting ions into metal oxide layered framework with concomitant reduction/oxidation of V atoms.

## CONCLUSIONS

In this work, we show that electrochemical synthesis is a method of choice for preparation of nanoscale architectures that require electronic conductivity, and it eliminates the need for conductive carbon additives and binders typically used in electrodes that alter their long-term stability. In addition, the electronically interconnected porosity of the electrochemically prepared nanoscale organized electrodes allows excellent ion transport while the large surface area provides an electrochemically active surface that is not constrained by diffusion limitations. It is at the nanoscale that near theoretical capacity and high-power electrodes can be achieved using simple self-organization processes. We show the ability of the open frame layered structure to accommodate for a large volume of Na ions by adjusting the layer spacing upon exposure of reduced layered structure to a high concentration of Na ions. The electrostatic attraction of electrochemically altered vanadium oxide layers provides a strong driving force for the diffusion of a large concentration of transporting ions into the open layer frameworks. This consequently leads to ordering of the overall structure with appearance of both short-range order within the layers and long-range order between the layers. Upon deintercalation of sodium, the long-range order is lost while intralayer structure is still preserved. Inducing ordering of nanomaterials *in operando* allows realization of the highest possible electrode capacity by optimizing the balance of electrostatic forces. We developed a nanoscale ordered bilayered $V_2O_5$ cathode that operates at room temperature above the theoretical capacity of 250 mAh/g, with redox potentials of 3 V, giving an energy density of ~760 Wh/kg. The small diffusion length and large surface area of nanostructures also enable fast charging of $V_2O_5$ leading to high power of 1200 W/kg at a cycling rate of *C*/8. We believe that the small thickness of the bilayered structure is also responsible for improved elasticity and exceptional long-term stability of this open frame structure making bilayered $V_2O_5$ a suitable cathode material for high-energy density rechargeable sodium batteries.

## METHODS

**Synthesis of Nanostructured $V_2O_5$ Electrodes.** Nanostructured $V_2O_5$ was synthesized by electrochemical deposition on pure Ni foil (0.0127 mm, 99.8%), which was cleaned in acetone and isopropyl alcohol. The electrochemical deposition was carried out in a three-electrode cell with Ni foil as the working electrode, Pt mesh as a counter electrode, and Ag/AgCl as a reference electrode in aqueous 0.1 M $VOSO_4$ solution. Bilayered $V_2O_5$ electrodes were synthesized by vacuum annealing at 120 °C for 20 h. The crystallized orthorhombic $V_2O_5$ electrodes were obtained by annealing of as-prepared $V_2O_5$ under $O_2$ atmosphere at 500 °C for 4 h.

**Electrochemical Insertion/Extraction of $Na^+$ and Characterization.** Sodium half-cells were assembled in a He-filled dry glovebox into coin-type cells with a Na foil as the negative electrode, an electrolyte of 1 M $NaClO_4$ in propylene carbonate (PC), and glassy fiber separator. For comparison, a traditional electrode was made by mixing 84 wt % active material ($V_2O_5$ powder, Aldrich), 4 wt % graphite (Timcal, SFG-6), 8 wt % poly(vinylfifluoride) binder (Kynar), and 4 wt % carbon black (Toka) and pressed on stainless steel mesh current collector. All cells were tested galvanostatically by automated Maccor battery tester at ambient temperature. Cyclic voltammograms of the cells were recorded in a Solartron 1470E potentialstat/galvanostat.

**Synchrotron XRD Measurements.** X-ray diffractions were performed at the beamline 13-ID-D of GSECARS sector at Advanced Photon Source (APS) at Argonne National Laboratory. The X-ray beam (37 keV energy, corresponding to X-ray wavelength of $\lambda$ = 0.3344 Å) was focused to a 2 $\mu$m diameter spot with a Kirkpatrick–Baez mirror system. The distance and tilting of the MAR165-CCD detector were calibrated using a $CeO_2$ standard. $V_2O_5$ samples were prepared by stripping the $V_2O_5$ film from Ni support onto Kapton tapes. Electrodes removed from cells for analysis were thoroughly washed with dry dimethyl carbonate and dried under inert atmosphere. The charged samples were also prepared by stripping $V_2O_5$ films onto Kapton tape. The discharged samples were scratched-off and sealed inside a 3 mm diameter hole in a piece of aluminum foil by sealing the Kapton sheet to the foil using epoxy. All cell operations were performed in a He-filled dry glovebox (oxygen level <2 ppm). Simulations of XRD patterns were carried out using CrystalMaker (CrystalMaker Software, Ltd.).

**Synchrotron SAXS/WAXS Measurements.** SAXS/WAXS data were collected at Beamline 12ID-B of the Advanced Photon Source (APS) at the Argonne National Laboratory (ANL). The X-ray was focused, and the spot size on the sample was ~50 $\mu$m × 50 $\mu$m. SAXS and WAXS data were presented in momentum transfer, $q$ ($q = 4\pi \sin\theta/\lambda$, where $\theta$ is one-half of the scattering angle, and $\lambda$ = 1.033 Å is the wavelength of the 12 keV energy probing X-ray), measured in the range of 0.01–2.3 $Å^{-1}$. The charged samples were prepared by stripping $V_2O_5$ films onto Kapton tape. The discharged samples were scratched-off and sealed inside a 3 mm diameter hole in a piece of aluminum foil by sealing the Kapton sheet to the foil using epoxy. All cell assembly and disassembly operations were performed in a He-filled dry glovebox (oxygen level <2 ppm).

**XPS.** Scienta hemispherical electron analyzer (SES100) was used to perform the XPS/UPS measurements, and total energy resolution of spectra, including photon energy, was set to less than ~0.1 eV. The acceptance angle for incoming electrons is 5°. All experimental data were taken under the pressure of $2 \times 10^{-10}$ Torr or less.

**Electron Microscopy.** Scanning electron microscopy (SEM) images were recorded with a JEOL JSM-7500F field emission SEM operating at 30 kV. HRTEM images were recorded on JEOL EM-2100F.

**X-Ray Spectroscopy (XAS).** XAS and extended X-ray absorption fine structure (EXAFS) measurements were performed at PNC-XOR bending magnet beamline (20-BM-B) of APS in

Argonne National Laboratory. Measurements at V *K*-edge were performed under transmission mode using gas ionization chambers to monitor the incident and transmitted X-ray intensities. A third ionization chamber was used in conjunction with a V-foil standard to provide internal calibration for the alignment of the edge positions. The incident beam was monochromatized using a Si(111) double crystal fixed-exit monochromator. Harmonic rejection was accomplished using a rhodium-coated mirror. The charged samples were prepared by stripping $V_2O_5$ films onto Kapton tape. The discharged samples were scratched-off and sealed inside a 3 mm diameter hole in a piece of aluminum foil by sealing the Kapton sheet to the foil using epoxy. All cell assembly and disassembly operations were performed in a He-filled dry glovebox (oxygen level <2 ppm). The reference standards ($V^{5+}$ and $V^{4+}$) were prepared by spreading thin, uniform layers of the $V_2O_5$ and $VO_2$ power in Kapton tape and stacking a few layers to attain the desired absorption step height. Each spectrum was normalized using data processing software package IFEFFIT.[30] Alignment of each sample reference spectrum with respect to V standard spectrum is within the range of $\pm$0.03 eV.

*Acknowledgment.* The authors would like to thank Dr. Yuzi Liu for HRTEM measurements and useful discussions. This work was supported by the U.S. Department of Energy, U.S. DOE-BES, under Contract No. DE-AC02-06CH11357. Use of the Center for Nanoscale Materials and Advanced Photon Source was supported by the U.S. Department of Energy, Office of Science, Office of Basic Energy Sciences, under Contract No. DE-AC02-06CH11357. Work at sector 20 and research at these facilities supported by the U.S. DOE, NSERC (Canada), and Sector 13 GeoSoilEnviroCARS by the National Science Foundation-Earth Sciences (EAR-0622171) and Department of Energy-Geosciences (DE-FG02-94ER14466).

*Supporting Information Available:* Supplementary TEM, SEM, and XPS data are included. This material is available free of charge *via* the Internet at http://pubs.acs.org.

## REFERENCES AND NOTES


1. Li, G. C.; Li, Z. H.; Zhang, P.; Zhang, H. P.; Wu, Y. P. Research on a Gel Polymer Electrolyte for Li-Ion Batteries. *Pure Appl. Chem.* **2008**, *80*, 2553–2563.
2. Croce, F.; Appetecchi, G. B.; Persi, L.; Scrosati, B. Nanocomposite Polymer Electrolytes for Lithium Batteries. *Nature* **1998**, *394*, 456–458.
3. Wang, Y.; Takahashi, K.; Lee, K.; Cao, G. Z. Nanostructured Vanadium Oxide Electrodes for Enhanced Lithium-Ion Intercalation. *Adv. Funct. Mater.* **2006**, *16*, 1133–1144.
4. Sun, D.; Kwon, C. W.; Baure, G.; Richman, E.; MacLean, J.; Dunn, B.; Tolbert, S. H. The Relationship between Nanoscale Structure and Electrochemical Properties of Vanadium Oxide Nanorolls. *Adv. Funct. Mater.* **2004**, *14*, 1197–1204.
5. Zhai, T. Y.; Liu, H. M.; Li, H. Q.; Fang, X. S.; Liao, M. Y.; Li, L.; Zhou, H. S.; Koide, Y.; Bando, Y.; Goberg, D. Centimeter-Long $V_2O_5$ Nanowires: From Synthesis to Field-Emission, Electrochemical, Electrical Transport, and Photoconductive Properties. *Adv. Mater.* **2010**, *22*, 2547–2552.
6. West, K.; Zachauchristiansen, B.; Jacobsen, T.; Skaarup, S. Lithium Insertion into Vanadium Pentoxide Bronzes. *Solid State Ionics* **1995**, *76*, 15–21.
7. Zou, C. W.; Yan, X. D.; Han, J.; Chen, R. Q.; Gao, W. Microstructures and Optical Properties of Beta-$V_2O_5$ Nanorods Prepared by Magnetron Sputtering. *J. Phys. D: Appl. Phys.* **2009**, *42*, 145402–145407.
8. Velazquez, J. R.; Banerjee, S. Catalytic Growth of Single-Crystalline $V_2O_5$ Nanowire Arrays. *Small* **2009**, *5*, 1025–1029.
9. Yan, B.; Liao, L.; You, Y. M.; Xu, X. J.; Zheng, Z.; Shen, Z. X.; Ma, J.; Tong, L. M.; Yu, T. Single-Crystalline $V_2O_5$ Ultralong Nanoribbon Waveguides. *Adv. Mater.* **2009**, *21*, 2436–2438.
10. Pan, A. Q.; Zhang, J. G.; Nie, Z. M.; Cao, G. Z.; Arey, B. W.; Li, G. S.; Liang, S. Q.; Liu, J. Facile Synthesized Nanorod Structured Vanadium Pentoxide for High-Rate Lithium Batteries. *J. Mater. Chem.* **2010**, *20*, 9193–9199.
11. Matsuda, A.; Higashi, Y.; Tadanaga, K.; Minami, T.; Tatsumisago, M. Electrophoretic Deposition of Sol−Gel Derived $V_2O_5$ Microparticles and Its Application for Cathodes for Li-Secondary Batteries. *Key Eng. Mater.* **2006**, *314*, 107–111.
12. Xiong, C. R.; Aliev, A. E.; Gnade, B.; Balkus, K. J. Fabrication of Silver Vanadium Oxide and $V_2O_5$ Nanowires for Electrochromics. *ACS Nano* **2008**, *2*, 293–301.
13. Li, X. X.; Li, W. Y.; Ma, H.; Chen, J. Electrochemical Lithium Intercalation/Deintercalation of Single-Crystalline $V_2O_5$ Nanowires. *J. Electrochem. Soc.* **2007**, *154*, A39–A42.
14. Chou, S. L.; Wang, J. Z.; Sun, J. Z.; Wexler, D.; Forsyth, M.; Liu, H. K.; MacFarlane, D. R.; Dou, S. X. High Capacity, Safety, and Enhanced Cyclability of Lithium Metal Battery Using a $V_2O_5$ Nanomaterial Cathode and Room Temperature Ionic Liquid Electrolyte. *Chem. Mater.* **2008**, *20*, 7044–7051.
15. Tang, P. E.; Sakamoto, J. S.; Baudrin, E.; Dunn, B. $V_2O_5$ Aerogel as a Versatile Host for Metal Ions. *J. Non-Cryst. Solids* **2004**, *350*, 67–72.
16. Poizot, P.; Laruelle, S.; Grugeon, S.; Dupont, L.; Tarascon, J. M. Nano-Sized Transition-Metaloxides as Negative-Electrode Materials for Lithium-Ion Batteries. *Nature* **2000**, *407*, 496–499.
17. Larcher, D.; Bonnin, D.; Cortes, R.; Rivals, I.; Personnaz, L.; Tarascon, J. M. Combined XRD, EXAFS, and Mossbauer Studies of the Reduction by Lithium of $\alpha$-$Fe_2O_3$ with Various Particle Sizes. *J. Electrochem. Soc.* **2003**, *150*, A1643–A1650.
18. Tarascon, J. M.; Armand, M. Issues and Challenges Facing Rechargeable Lithium Batteries. *Nature* **2001**, *414*, 359–367.
19. Cao, Y. L.; Xiao, L. F.; Wang, W.; Choi, D. W.; Nie, Z. M.; Yu, J. G.; Saraf, L. V.; Yang, Z. G.; Liu, J. Reversible Sodium Ion Insertion in Single Crystalline Manganese Oxide Nanowires with Long Cycle Life. *Adv. Mater.* **2011**, *23*, 3155–3158.
20. Liu, H. M.; Zhou, H. S.; Chen, L. P.; Tang, Z. F.; Yang, W. S. Electrochemical Insertion/Deinsertion of Sodium on $NaV_6O_{15}$ Nanorods as Cathode Material of Rechargeable Sodium-Based Batteries. *J. Power Sources* **2011**, *196*, 814–819.
21. Su, L. Y.; Winnick, J.; Kohl, P. Sodium Insertion into Vanadium Pentoxide in Methanesulfonyl Chloride-Aluminum Chloride Ionic Liquid. *J. Power Sources* **2001**, *101*, 226–230.
22. Petkov, V.; Trikalitis, P. N.; Bozin, E. S.; Billinge, S. J. L.; Vogt, T.; Kanatzidis, M. G. Structure of $V_2O_5$ $n$$H_2O$ Xerogel Solved by the Atomic Pair Distribution Function Technique. *J. Am. Chem. Soc.* **2002**, *124*, 10157–10162.
23. Petkov, V.; Billinge, S. J. L.; Larson, P.; Mahanti, S. D.; Vogt, T.; Rangan, K. K.; Kanatzidis, M. G. Structure of Nanocrystalline Materials Using Atomic Pair Distribution Function Analysis: Study of $LiMoS_2$. *Phys. Rev. B* **2002**, *65*, 092105–092109.
24. Shobu, T.; Noda, Y.; Ninomiya, E.; Sawa, H.; Nagamatsu, S.; Fujikawa, T.; Ueda, Y.; Isobe, M.; Ikeda, N.; Uruga, T. XANES Study of Charge Ordering on the Spin-Peierls Phase Transition of $\alpha'$-$NaV_2O_5$. *J. Synchrotron Radiat.* **2001**, *8*, 746–748.
25. Donsanti, F.; Kostourou, K.; Decker, F.; Ibris, N.; Salvi, A. M.; Liberatore, M.; Thissen, A.; Jaegerman, W.; Lincot, D. Alkali Ion Intercalation in $V_2O_5$: Preparation and Laboratory Characterization of Thin Films Produced by ALD. *Surf. Interface Anal.* **2006**, *38*, 815–818.
26. Mansour, A. N.; Smith, P. H.; Baker, W. M.; Balasubramanian, M.; McBreen, J. A Comparative *In Situ* X-ray Absorption Spectroscopy Study of Nanophase $V_2O_5$ Aerogel and Ambigel Cathodes. *J. Electrochem. Soc.* **2003**, *150*, A403–A413.
27. Giorgetti, M.; Berrettoni, M.; Passerini, S.; Smyrl, W. H. Absorption of Polarized X-rays by $V_2O_5$-Based Cathodes for Lithium Batteries: An Application. *Electrochim. Acta* **2002**, *47*, 3163–3169.
28. Liu, H. M.; Wang, Y. G.; Li, L.; Wang, K. X.; Hosono, E.; Zhou, H. S. Facile Synthesis of $NaV_6O_{15}$ Nanorods and Its Electrochemical Behavior as Cathode Material in Rechargeable Lithium Batteries. *J. Mater. Chem.* **2009**, *19*, 7885–7891.
29. Arico, A. S.; Bruce, P.; Scrosati, B.; Tarascon, J. M.; Van Schalkwijk, W. Nanostructured Materials for Advanced Energy Conversion and Storage Devices. *Nat. Mater.* **2005**, *4*, 366–377.
30. Newville, M. IFEFFIT: Interactive XAFS Analysis and FEFF Fitting. *J. Synchrotron Radiat.* **2001**, *8*, 322–324.